Compact Laser Driver for Ultrasonic Arbitrary Position and Width Pulse Sequences Generation

Linas Svilainis, *Senior Member, IEEE*, Andrius Chaziachmetovas, Valdas Eidukynas,
Arturas Aleksandrovas, and Marijus Varatinskas

Abstract—Laser ultrasound offers several benefits in comparison to immersion or air-coupled ultrasound: it directly generates stress on the sample surface; it has a wide bandwidth and a small acoustic source can be produced. Conventionally, high-power pulsed lasers are required therefore equipment is bulky and expensive. Here we propose to use mid-power laser diodes, which are small and low cost. To solve the low signal amplitude problem with lower power lasers, the use of spread spectrum signal, arbitrary position, and width binary pulse sets is proposed. To date, a laser driver for this task has not been available. This article describes the development of such a compact driver, where the essential electronics occupy an area of 10 × 20 mm. The whole system with a fixture for kinematic mount is comparable in size to a conventional piezoelectric ultrasonic transducer. The driver can supply pulse sets of up to 40 A. Individual pulse duration can vary between 20 and 1000 ns (0.5–25-MHz ultrasound range) and the total pulse train duration is limited by the laser type used. Experiments show that up to 10-μs long pulse sets can be used at 10-A current, without laser degradation. Current waveforms, beam profile, and optical response signals were measured for three rectified topologies. It was concluded that the GaN-based constant current switch topology has the best performance, but a power MOSFET in a source current feedback topology can also be used to generate pulses down to 20 ns. Photoacoustic response signals from chirp and phase shift keying modulation have been demonstrated.

Index Terms—Arbitrary position and width pulse (APWP) sequences, acoustic point source, diode lasers, laser ultrasound, laser driver, thermoelastic regime, ultrasonic transducers.

I. INTRODUCTION

ULTRASONIC measurement and imaging are used widely across a range of application areas. One of the outstanding ultrasonic equipment features can be the small size, low cost of transducers, and the absence of ionizing radiation [1]. However, the bandwidth is limited if a conventional, piezoelectric transducers are used [2]–[4]. Unfortunately, the efficient energy transmission into the test media requires a piezoelectric transducer to be in contact with the test medium. Noncontact transduction is possible using air-coupled ultrasound which can be challenging with high impedance mismatches, or electromagnetic acoustic transducers (EMATs) which while being noncontact still must be within a few millimeters of the sample surface [5]–[7].

Laser ultrasound, which was first proposed 60 years ago [8], offers several benefits in comparison to immersion or air-coupled ultrasound [9]–[13] for some applications. First of all, it is directly coupled to the surface of the test sample so: 1) acoustic contact is stable [14]; 2) components that are sensitive to water can be inspected [15]; 3) impedance mismatch does not affect the signal level [11]; 4) reverberation in coupling media as observed with some contacting transducers is avoided; and 5) accurate transducer focal point and test sample alignment is not necessary [16]. Other advantages are that acoustic source is not resonant, so that wide bandwidth is possible [10]; the distance from the light source to the test sample can be large [13]; arbitrary shapes of the acoustic source can provided using special optics [17]–[22]; and the probing point can be confirmed visually (if a visible light laser is used or via an IR camera).

Three regimes of ultrasound production via laser excitation can be identified [9]: 1) plasma or ablation regime uses $>=10^7$ W/cm^2 (for metal) [13], [23]; 2) thermoelastic $<10^7$ W/cm^2; and 3) intermediate [24].

Thermal expansion of the volume, heated by laser pulse is the major cause of the ultrasound production in the thermoelastic regime, where incident power densities are below the damage threshold of the test material [25]–[27]. The amplitude of the acoustic waves produced (longitudinal, shear, and Rayleigh) is proportional to the energy absorbed from the laser beam [25]–[28].

More mechanisms produce ultrasonic waves in plasma regime: light pressure, thermal expansion, electrostriction, and material ablation recoil [9], [10], [29]. Very high amplitude signals, into nonlinear ranges of ultrasound, can be obtained [10], [30]. It is sometimes essential that a longitudinal wave propagating normal to the surface is produced, but the

resultant wave can have complex and wide beam directivity. Laser ablation can also change the material surface, so subsequent signals are different if obtained in the same location [9] and material damage occurs, particularly where coating or surface layers with different properties to the bulk are removed by the first laser beam shot.

Another problem, related to the thermoelastic regime laser ultrasound is the production of dual acoustic pulse when the free surface thermoelastic source is used. Transient heating of the material surface produces two pulses, which travel in opposite directions: one toward the material bulk and another outwards. This second pulse is reflected back into material. The distance between the pulses is small, usually just the laser penetration depth (5–10 nm for metals [10]). In such case, the second pulse almost immediately (fractions of nanosecond) cancels the first pulse. Therefore, the generation of longitudinal waves normal to the material surface is complicated in the thermoelastic regime. There are applications that make use of the angled or surface waves [14], [31]–[35], and others that require the main beam to be directed normal to the surface. In these cases, a constrained (buried) laser ultrasound source can be considered (sometimes addressed as fourth regime in laser ultrasound). In this case, the surface is either coated with an optically transparent layer on top of the sample, resulting in constrained acoustic source [36]–[45]. Then second pulse is either delayed or canceled, giving rise to the longitudinal wave propagating normal to the surface being enhanced by several orders when compared to the unconstrained surface. When a transparent coating is applied to the surface of the probed material, a second ultrasonic pulse travels in the coating until it is reflected back from the air interface. If the coating thickness is comparable to the ultrasound wavelength and the attenuation in coating is low, then resonant effects can be observed. The presence of the coating also reduces the amplitude of the surface wave, which is usually induced in unconstrained surface [41]. A constrained surface is considered in this article.

When excited by a single pulse, the resulting signal lacks high frequencies and there are spectral dips because of the *sinc* shape of the spectrum. Excitation using the spike somehow leverages the problem, but the amount of energy per bandwidth of interest is very low. The wider is the required bandwidth, the higher is the desired frequency for excitation, the shorter should be the pulse duration. A large excitation power then has to be used to counter the lack of energy. This in turn calls for the bulky and expensive laser source. Then the essential ultrasound advantages like safety, small size, and low cost are lost.

Spread spectrum (SS) excitation can solve the challenge of using a generation source with low-pulse energy because bandwidth is not related to the pulse duration for SS signals [3]. While widely used in conventional ultrasonic techniques, the SS application for use with laser ultrasound is complicated.

A CW laser (100 mW to 2-W power) can be modulated by a SS signal, which after reception can be compressed in software [46]–[52]. However, the power transmitted is very low, and the thermoelastic wave produced is small, so significant averaging of very long SS signals has to be used; the modulation is shallow and all the equipment is analog, so that efficiency suffers.

There is an intermediate solution, which has all the conditions required for successful exploitation in laser generated ultrasound: mid-power ultrasound, using binary sequence excitation. Laser diodes of 10 W or even 600-W pulse power, which are now off the shelf components. Pulse durations in the range of 10–1000 ns are possible, which fits well onto the range required for 0.5–50-MHz ultrasound generation. The complexity of the optics required is reduced, thanks to the wide availability of relatively low-cost aspheric lenses. The only missing element required to create a small laser ultrasound source is the laser driver. If all the components can fit into the size of the conventional ultrasonic transducer (approximately 50-mm long, 20-mm diameter) and at a comparable price, then the development of mid-power laser ultrasound will lead to many applications. There are many applications for such medium power lasers [53]–[63], mainly in photoacoustic imaging, where only a single-pulse excitation is usually used.

There have been previous attempts to use SS excitation using mid-power (100 W) pulsed laser [64], but researchers had to use emulation, due to the unavailability of a fast, high current laser driver for generating pulse sequences. The acoustic response to a single pulse was measured and then pulse sequences were produced artificially, emulating SS sequence excitation.

In this work, we present the development of the complete laser ultrasound source. Targeted applications are the synthetic aperture focusing technique (SAFT) [10], [65]–[68], photoacoustics [53]–[63], and the transducer spatial sensitivity evaluation and calibration [69]–[72]. The whole laser system is compact and lightweight. It is capable of generating a small (down to 100 μm) acoustic source of arbitrary position and width pulse (APWP) sequences [69] (i.e., not a single pulse but multiple pulse trains).

The majority of the research effort was concentrated on developing the driver electronics. The beam shape control was limited to a simple optics, aiming for simplicity and small size. The experimental investigation of the ultrasound generation on an acoustic delay line is presented, demonstrating that the spectral content of the ultrasonic signal can be controlled using the APWP sequences, described in [69] and [73].

II. REQUIREMENTS STUDY

There are certain limitations that have to be considered when efficient ultrasound excitation in the thermoelastic mode is used: 1) the limited available power and 2) the requirement for a wide range of pulse durations and their repetition frequency.

A. Attainable Power Density

Power density used in high-power ultrasound usually is close to the ablation threshold, 10^5–10^7 W/cm^2 [9], [10], [31]–[45]. The peak power has to be from tens of kW (42 kW in [53]), to hundreds of kW ([74], 833 kW in [43], 555 kW in [41], 300 kW in [19], 384 kW in [21]) or even MW (1.25 MW in [75], 1.7 MW in [36]). Usually researchers aim to use large (mm order) laser spot because this increases longitudinal waves energy directed normal to the surface, but power densities remain in MW/cm^2 range.

TABLE I

LASER DIODES USED IN THE INVESTIGATION

Model	P_{max}, W	Aperture, μm	I_{max}, A	V_F, V	Θ_{FWHM}, deg
SPL PL90_3	75	200x10	40	9	9/25
SPL UL90AT08	120	220x10	40	11	10/25
905D1S3J09UA	80	235x10	35	12.8	12/20

Laser diodes used in this study are mid-power (refer Table I: SPL UL90AT08, SPL PL90_3 are from OSRAM Opto Semiconductors GmbH, Regensburg, Germany and 905D1S3J09UA from Laser Components GmbH, Germany).

It is difficult to reach the aforementioned power density with a laser diode whose power is limited to 75–120 W. Assuming a 5-mm spot size and 120-W laser would result in a power density of 600 W/cm^2. However, we see the merit of the small spot size. If a 120-W beam is focused into a 200-μm diameter spot, the power density would be 380 kW/cm^2. Alternatively, a 75-W laser at a 100-μm spot diameter can produce 10^6 W/cm^2, which is close to the power densities that provide sufficient acoustic output (assuming 100% absorption). Many application can benefit from a small spot size: 1) a wide acoustic beam is required in SAFT imaging [65]–[68]; 2) if the material investigated is thin, then the acoustic beam can be considered already focused so high lateral resolution is attained [70]; 3) photoacoustic imaging requires small laser beam size [53]–[63]. However, laser beam spot size cannot be reduced indefinitely, and is usually limited by the emitting aperture size (10 μm × 200 μm is common) and the optical system magnification/reduction. The small laser beam spot size is supposed to result in a small acoustic generation spot size, but it could be larger [39].

B. APWP Sequence Parameters

Replacing the single-pulse excitation with APWP sequences offers several benefits. Long signals can be used, so signal energy is boosted not by increasing the instantaneous power (pulse amplitude) but by signal duration. Application of a matched filter (cross correlation function) allows one to compress the signal, obtaining a sharp pulse. The signal spectrum can be designed to match the required bandwidth, so that all of the energy is used to produce useful frequencies. Furthermore, the spectral content of the ultrasonic signal can be programmed [73]. APWP sequences can be considered as a binary analog of an arbitrary waveform. In this article, only laser ON or OFF states are available. According to signal theory, the optimal pulse duration is half of the period of the desired frequency component. When the conventional ultrasound range of 0.5–20 MHz is considered, the pulse durations should be from 25 to 1000 ns. Several well-known signals can be generated using APWP sequences: single pulse, CW toneburst, phase shift keying (PSK) sequences, chirp, or completely arbitrary pulse sequences. CW toneburst can have a fixed duty cycle and pulse repetition period equal to the desired frequency f_0, or a variable duty cycle to adjust the amplitude or impose an envelope modulation. For PSK sequences, the

chip (the elemental atom of a PSK sequence) is constructed following the toneburst principles: the pulse duration defines the bandwidth and the repetition frequency defines the center frequency. Chirp signals can be made using the linear or nonlinear frequency modulation (LFM or NLFM), it can have a tapered amplitude using duty cycle variation [73]. Arbitrary pulse sequences can adapt to the required spectral [73] or correlation properties [69] by optimization. The total sequence length is limited by the laser diode's safe operating conditions: at 40 A, it should be limited to around 500 ns, but for 10-A APWP sequence length can reach tens of μs.

III. LASER DRIVER DEVELOPMENT

Laser diodes are usually low-voltage devices, where the forward voltage is 5–12 V, even for stacked lasers. Therefore, a high current of up to 40 A is required to deliver the power required. Laser drivers that are commercially available are large and are not intended for relatively short duration and high intersymbol rate APWP sequences generation.

The laser driver PCO-7114-22-2 is available from DEI (Directed Energy, Inc., San Rafael, CA, USA), and is relatively small (62 × 38 mm), producing up to 22-A pulses, but can only produce a single pulse of a fixed <2-ns duration. The PCO-7110 driver can produce a 4–65 ns, 4–120-A pulse, but is not capable of driving sequences (pulse repetition frequency (PRF) is 50 kHz). The PCO-7120 (51 × 103 × 19 mm) can produce pulse widths of 12–1000 ns at 5–50-A per pulse, but the PRF is limited to 1 MHz. The laser driver BFS-VRM 03 offered by Laser Components (Laser Components GmbH, Olching, Germany) can produce a wide range of pulsewidth of 1 ns to CW output, with a size of 65 × 85 mm, yet the maximum output current is just 3 A. The same company offers the pulsed driver LSP-40, which can deliver 40 A, 30–1000-ns single pulsewidth (PRF is 10 kHz). Hamamatsu (Shidzuoka, Japan) offer a laser driver board C14518, that can deliver up to a 40-A pulse, but the single-pulse duration is fixed to 4 ns, and the PRF is limited to 150 kHz). Quantel have reported a laser driver capable of 1.7 mJ, but again, the pulse output is single and a fixed 40-ns duration [53]. To summarize, commercially available drivers offer just a single pulse and are mostly aimed for short, <10 ns, pulse generation.

Short laser pulses are of interest in lidar, and there has been significant effort in laser drivers development for this purpose [76], [77], [78]. Yet, the solutions proposed are either too low power and pulse durations are not within the range of interest discussed here, or the PRF is too low. Section III-C provides a more detailed discussion on topologies.

To conclude, conventional pulsed laser drivers are aimed at generating single short pulses, but the application presented in this article requires wide range, of pulsewidth of up to 1000-ns duration and repetition frequency close to 30 MHz. The driving current should reach its "ON" state as fast as possible, and should be maintained over the whole duration of the pulse.

A. Main Switch FET

The selection of the FETs used in the main switch was based on maximum current (40 A from Table I) and

TABLE II
FETs USED IN INVESTIGATION

Model	V_{DSmax}, V	I_{Dmax}, A	Q_{Gtot}, nC	C_R, pF	C_G, pF	C_{outMax}, pF
EPC2019	200	42	1.8	0.7	200	380
NVTFS6H888N	80	47	4.7	3	220	320
BSZ340N08NS3	80	92	6.8	7	470	600
BSZ146N10LS5	100	176	15	9	1000	1000
BSZ900N15NS3	150	52	5	3	380	600

TABLE III
FET DRIVERS USED IN INVESTIGATION

Model	V_{out}, V_{min}	I_{out}, A	R_{out}, Ω	t_{Dly}, ns	t_R, ns
LMG1020	4.3-5.4	7/5	n.a.	2.5	0.37/0.35
UCC27511	4.2-18	4/8	5/0.45	10/12	7.5/5
MAX5048	4-14	7/3	0.88/0.32	8	5/4
ISL55110	0-14	3.5	3	10	1.2/1.4

maximum speed. A smaller reverse capacitance C_R reduces the parasitic feedback (oscillations). Total gate charge Q_{Gtot} (together with gate driver current I_{out} capability) and gate capacitance C_G define the turn-on speed. The FET output (drain–source) capacitance C_{outMax} at 0-V drain–source voltage, influences the switching losses, oscillation, and edge duration. The drain–source breakdown voltage V_{DSmax}, defines the attainable compliance voltage (40–50 V were required; see Section C). Two FET types were selected (refer Table II): the most popular enhancement mode GaN (EPC2019 in 2.7×0.9 mm wafer-level chip scale package (WLCSP), from Efficient Power Conversion Corporation, El Segundo, CA, USA) and a power MOSFET (NVTFS6H888N in WDFN8 3×3 mm package from ON Semiconductor, Phoenix, AZ, USA; BSZ340N08NS3, OptiMOS3 and BSZ146N10LS5, OptiMOS5 in 3×3 mm TSDSON-8 package from Infineon Technologies AG, Neubiberg, Germany).

While GaN is the obvious choice, it has some disadvantages: 1) the gate voltage range is very narrow, so that gate boosting might be dangerous (MOSFETs are more immune to gate transients, within the $\pm$ 20-V range, while GaN have only −4 to +6 V) and 2) the WLCSP package is difficult to solder manually and to inspect for soldering quality. Besides, it was interesting to investigate what parameters power MOSFET can achieve.

B. FET Driver

Four FET drivers were selected (refer Table III).

The LMG1020 (0.8×1.2 mm DSBGA package, from Texas Instruments Incorporated, Dallas, TX, USA) was chosen because of the low-propagation delay time and impressive rise/fall times (it should be noted that these are specified at very light, 100-pF load). Yet, this driver has a serious limitation: the available output voltage range is very narrow. As will be seen in the following explanation, a regulated driver output voltage was required. The UCC27511 (SOT23 package, from Texas Instruments Incorporated, Dallas, TX, USA) and MAX5048 (SOT23 case, from Maxim Integrated, San Jose,

CA, USA) drivers have similar performance, with one essential difference: MAX5048 can source up to 7 A and has much lower (0.88 Ω) source impedance, while the UCC27511 is almost the opposite, having a high (8 A) sink current. The ISL55110 (TSSOP package, from Maxim Integrated, San Jose, CA, USA) is a special case, and is particularly suited to the application discussed in this article: it has separate power supplies for the internal logic and the output stage. Therefore, it can provide very low output voltages without significant performance degradation (driver output FETs' driving voltage can stay fixed). It also has two channels in one package, which have been paralleled to get 1.5 Ω and 6-A output. Simulation using LT SPICE did not reveal significant differences in the drivers' performance, and so it was decided to concentrate on two drivers: the ISL55110, with two channels paralleled and the LMG1020 only for GaN in switch mode.

C. Parasitics

The inductance of the laser diode current loop, including the printed circuit board (PCB) [79], limits the rise time of the current injected. According to [80] the laser contributes most of the inductance, and the majority of the inductance comes from the laser package, including the wire bonds. The inductance value stated in [80] is 5 nH. Very short laser diode pins (2-mm long), were soldered directly on PCB to keep the laser inductance as low as possible. Our measurements indicate that in such a case, the inductance of the laser diode is 2.5 nH at 10-mA bias (measurements at higher currents were not done to avoid laser damage). Delivery of the high current pulses to a laser diode is also a challenge [80]: a microstrip type, low inductance transmission line has to be used, and this still introduces parasitics. Therefore, it was decided that the laser driver has to be integrated with the laser diode on the same PCB. The PCB trace also contributes significant inductance: a 1-mm wide, 10-mm long trace on 1.5-mm FR4 substrate would give 19 nH, so it was decided that wide traces and thin PCB would be used. The 1.5-mm PCB with 10-mm wide and 6-mm long trace would contribute 1.14-nH inductance, but an 0.8-mm PCB would have 0.47-nH inductance (0.9 nH if both forward and returning current path is considered). The MLCC capacitor, according to [81] has 870, 1050, and 1200 pH for the 0603, 0805, and 1206, respectively, while the inverted 0612 has 610 pH and the 0508 has 600 pH. The inverted MLCC case was used in the main current loop. Resistors have even higher parasitic inductance if in a standard configuration (resistive layer on top of ceramic substrate): wrap-around effect causes the 0603 to have 1600 pH and the 0402 to have 120-pH inductance [82]. Fortunately, flipped versions (resistive layer at the bottom) have 26.7 pH for the 0603 and 2 pH for the 0402. Several components can be used in parallel, further minimizing the parasitic inductance, yet it has been reported that five parallel 0402 shunt resistors flipped, still have 40-pH inductance [80]. Inverted and flipped case resistors were used in the main current loop.

FET manufacturers usually do not specify inductance, but data was available for the WDFN8 case (one used in this research): the drain inductance is 0.2 nH and the source inductance is 0.65 nH [75].
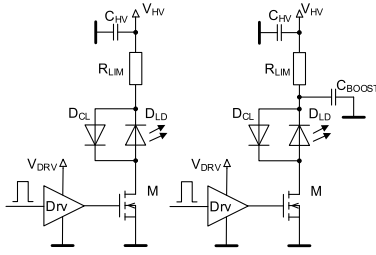
Fig. 1. Resistor current limiter topology (left) and boosted version (right).
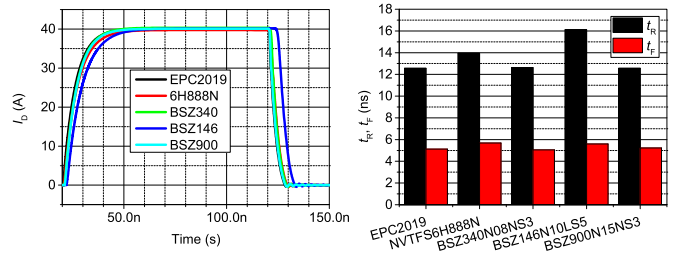

Fig. 2. Resistor current limiter topology driving current waveforms (left) and edge durations (right).

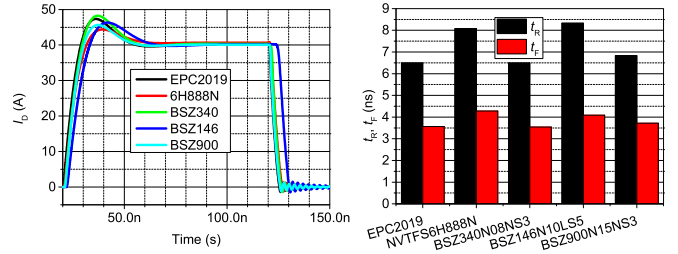Fig. 3. Boosted resistor current limiter waveforms (left) and speed (right).

The expected loop inductance, even considering the modifications mentioned is 4.6 nH. The required compliance voltage can be calculated from this inductance. A simplified equation for the rising edge is

$$t_R = \frac{dI \cdot L}{V} \tag{1}$$

where dI is current step size, V is the excitation voltage, L is the loop inductance, and t is time. If 25 ns is the shortest pulse to be produced, then t_R should be at least 5 ns. In such a case, a 40-A step requires 36 V. If the forward voltage of the laser diode is 9–12 V, then the compliance voltage should be within the 40–50-V range. It should be noted that this equation does not take into account that the MOSFET switch is a current sink at high V_{DS} voltages, and is a resistor at low voltages, so that actual rise times will be longer. Yet, there is an essential problem that can be seen from (1): a high compliance voltage is required to achieve fast rise time [83].

D. Driver Topologies Analysis

A circuit with resistor current limiter can be considered as the simplest one (Fig. 1, left).

Here, the laser diode current is defined by the voltage V_{HV}, laser diode forward voltage and limiting resistor R_{LIM}, plus the FET resistance R_{DS}. Moderate drive current stability can be achieved with a stable V_{HV} voltage and low FET temperature variation. The circuit is simple, and current monitoring can be done by measuring the voltage drop on the resistor R_{LIM}. A clamping diode D_{CL} is used for the FET M and laser diode D_{LD} protection, against the voltage transients caused by the cutoff of the high loop current.

This circuit has been simulated using LT SPICE, using 0.5 Ω R_{LIM} 40-V V_{HV}, and a 1.5 Ω gate driver (equivalent to two ISL55110 channels in parallel). The results are presented in Fig. 2.

The simulation used only one laser diode model, which had highest forward voltage. It was derived from the RLD90QZW3 (Rohm Semiconductor) model, which has similar parameters to the 905D1S3J09UA model. Simulation results indicate that 40-V V_{HV} is insufficient: only 12.5–16-ns rise times were obtained. The reason is very simple: the compliance voltage is less than V_{HV} by voltage drop on R_{LIM} (20 V) plus FET voltage (6 V for NVTFS6H888N and BSZ900N15NS3, 1.6 V for EPC2019, 1.2 V for BSZ340N08NS3, or 0.5 V for BSZ146N10LS5 at 40 A).

The circuit can be easily boosted to give more current during the rise time (Fig. 1, right), and the boosted topology has been
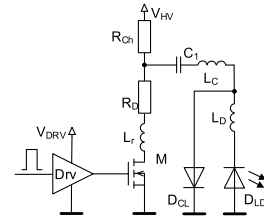

Fig. 4. Capacitor discharge/resonant laser diode drive topology.

simulated using C_{boost} 15 nF and V_{HV} 40 V, results are in Fig. 3.

From this simulation, it can be concluded that the rising edge duration has been reduced significantly, down to 6 ns and all FETs have similar performance. Higher V_{HV} (and larger R_{LIM}) would allow for further switching time reduction. The fact that the NVTFS6H888N performance is slightly worse than that for the BSZ900N15NS3 is unexpected, as these MOSFETS have similar parameters. Notable, that the falling edge times were also reduced (from 5 to 3.5 ns). The boosted resistor current limiter was selected as the candidate with GaN FET EPC2019.

The driver described in [84] is based on a standard capacitor discharge topology. It has a small footprint (50 × 50 mm), and can only reach 10 A with 1–1.5-ns single pulse widths at 100-kHz PRF, and a compliance voltage of up to 150 V is required. Circuit (Fig. 4) can be modified as in [78] and [80] so that its performance becomes similar to the boosted resistor current limiter topology (Fig. 1, right), and only R_{lim} and C_1 have different function and values here.

Here, capacitor C_1 is charged via the $R_{Ch} - D_{CL}$ network. Turning on, switching the M will cause the C_1 to discharge into the laser diode D_{LD}. The circuit is usually made resonant
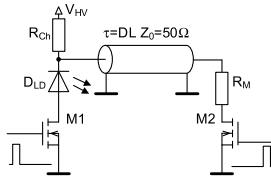
Fig. 5. Charge-line dual FET laser diode drive topology.

Fig. 6. Inductive boost laser diode drive topology.

Fig. 7. FET acting as both switch and current sink laser diode drive topology.

so the resulting pulsewidth is [76]

$$\tau_{0.5} \approx 2 \cdot \sqrt{L_\Sigma \cdot C_1} \qquad (2)$$

where L_Σ is the total loop inductance (usually formed just by series connection of the PCB parasitics, L_r is the capacitor stray inductance and L_C is the inductance of the laser diode L_D).

The peak current of the laser diode is defined by V_{HV}, C_1, and L_Σ if circuit is optimally damped [76]

$$I_{pk} \approx \frac{V_{HV}}{R_D \cdot \sqrt{\frac{L_\Sigma}{C_1}}}. \qquad (3)$$

A major disadvantage of such a circuit is that pulse duration and current depend on parasitics and the C_1 parameters, so it is not suitable for producing a wide range of pulse durations. Furthermore, a large C_1 is required for long pulses, making charging time very long, which is why this topology usually has only Hz to kHz range PRF. Another aim of the research described in this article is to develop a circuit suitable for PRF of up to 30 MHz, within the sequence. The PRF can be increased using very low R_{Ch} values, but it will affect the resonant tank and severely increase the load on switch M.

The same solution is used in [85], where a GaN FET can deliver up to 30 A, 0.5–25-ns wide pulses at a PRF of up to 5 MHz, or 60 A, 50–500-ns wide single pulse as per [86]. Mode-locked lasers [87] can reach 100-MHz PRF, even at 20-A, but pulses are short (<2 ns) and the PRF is fixed: this solution is not suitable for APWP sequences. The laser driver presented in [85] uses GaN transistors, and can deliver 400 A, but only for a 50-ns wide single pulse.

An interesting solution was described in [89], using a delay line with a variable load (Fig. 5). It can achieve current only up to 1.2 A, at a 20-MHz PRF and 200 ps up to 2-ns pulse widths.

Here the delay line, charged via R_{Ch} together with switch M2 is used to control the pulse duration. The current is mainly defined by the ratio of VHV and Z0, so that only low currents can be developed. Furthermore, the pulsewidth maximum duration is defined by the delay line delay value DL, so that a very long delay line would be needed, to achieve pulse widths of 1000 ns.

The inductive boost topology (Fig. 6) uses an inductance L_{Ch} (could also be PCB trace), precharged by a constant current source I_{cc}, to immediately set the compliance voltage that is required to drive laser diode parasitic inductance. The laser diode is always tampered by M, and when a current pulse is required, the current accumulated in L_{Ch} is released into D_{LD}, to generate a fast rising edge.
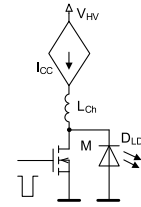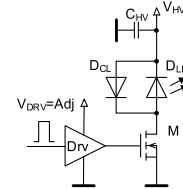
A similar solution presented in [90] is very attractive and energy-efficient: a constant current is produced by a dc/dc converter, that can achieve 2.5-MHz PRF at 5 A, but requires three switches and complex driving signals, which should be implemented in dedicated IC or FPGA.

The avalanche bipolar junction transistors can produce high-power pulses, but pulse widths are short and the topology requires high voltage (300 V in [91]).

An interesting capacitive boosting solution is described in [92], where a switched capacitance is used to provide extra compliance voltage during the current rise time. The solution described can only achieve pulses up to 1 A, and pulse duration is limited by the capacitance used. It requires six switches and complex driving logic. The circuit in Fig. 1, right can be considered to be a simplified version of this idea. A capacitive charge transfer and voltage doubler combination is presented in [93], which can achieve impressive 330-MHz PRF, but current is limited to 180 mA, with a pulsewidth of 252 ps.

The laser driver presented in [94] uses an innovative resonant laser drive to deliver fixed a 20-A current at a PRF of up to 40 MHz, but the pulsewidth duration is short and fixed to 1 ns. Resonant driving is also used in [95] to achieve a current of 35 A and pulse widths below 4 ns, in comparison with BSZ146N10LS5, which is done by simulation. The topology inherently limits pulse duration and PRF. The laser driver presented in [96] is capable of a 100-MHz PRF, but the pulsewidth is fixed at 5 ns and has a peak current of only 2 A. The same resonant drive can achieve a current of 150 A for a fixed 8-ns wide single pulse [97]. The design described in [98] is an integrated solution, using the current sink topology, and can deliver up to 80 A, but only up to 25-ns single pulse. A similar approach [99] achieved a current of 10 A for a single 10–50-ns pulse. The low-side switch solution presented in [100] obtains pulse widths down to 2.5 ns at currents of up to 9 A, with a 200-MHz PRF and pulses with 1-ns rise and fall times. A new concept can be derived from the topologies discussed: the FET can act both as a switch and as a current sink (Fig. 7).
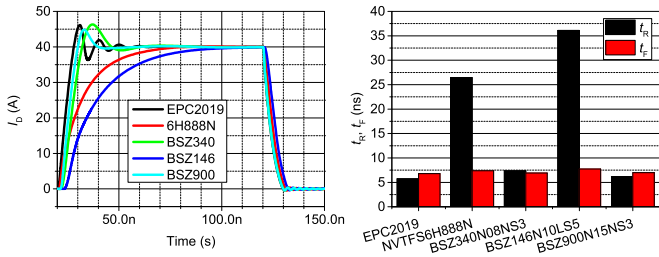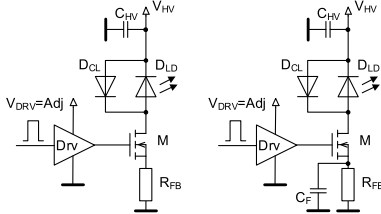
Fig. 8. FET current sink topology current waveforms (left) and speed (right).

Fig. 9. FET with source current feedback topology (left) and with filter capacitor to reduce parasitic L effects and boost the rising edge (right).

Fig. 10. FET source feedback current waveforms (left) and speed (right).

Fig. 11. Boosted FET source feedback waveforms (left) and speed (right).

MOSFETs are usually overdriven to ensure that lowest available channel resistance is achieved, but an FET driven at a certain given voltage behaves like a current sink. This property can be exploited to provide the pulsed laser current. The idea is not applicable to the topology of Fig. 4: a low R_{CH} has to be used and then M cannot be used to set the laser diode current, because the major current flow will be through R_{CH}. The topology shown in Fig. 7 has been simulated using LT SPICE, with a gate voltage selected for every FET individually. Results are presented in Fig. 8.

Simulation indicates, that new idea can be used, however, some MOSFETs are too slow. Whilst this is expected for BSZ146N10LS5 (gate charge and reverse capacitance are ten times larger than EPC2019), the results for NVTFS6H888N are quite unusual. The best rise times were for the EPC2019 (5.7 ns) and the BSZ900N15NS3 (6.2 ns). The FET (EPC2019) current sink topology was selected as the candidate.

However, such a topology is not immune to temperature effects, and so additional modification can be used such as source feedback (Fig. 9, left). This topology is usually used when a simple current sink is needed.

Feedback resistance R_{FB} can be chosen to provide few volts at maximum current. For a 40-A current and 100-mΩ R_{FB}, the feedback voltage would be 4 V. Such a low R_{FB} value becomes comparable to parasitic inductance: a 40-pH inductance can be expected, even if the flipped version is used [80]. It is not applicable to GaN FETs due to the high gate voltages used. A small filter capacitor C_F can be used in parallel to R_{FB} (Fig. 9, right) to smooth parasitic L effects during signal transitions. This capacitor can also serve as an edge booster: FET current is increased if V_{FB} is lowered. These topologies were simulated using LT SPICE with a 200-pH parasitic inductance for R_{FB}. Results are presented in Figs. 10 and 11.

The best rise times for the nonboosted versions was for BSZ340N08NS3 (6.5 ns) and BSZ900N15NS3 (6.7 ns). The boosted version (10-nF C_F) introduced oscillations for BSZ340N08NS3 (5 ns) and BSZ900N15NS3 (5.3 ns), though
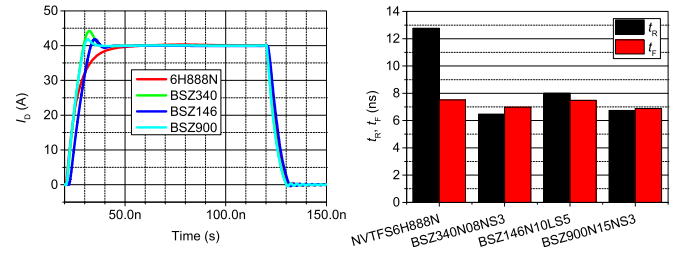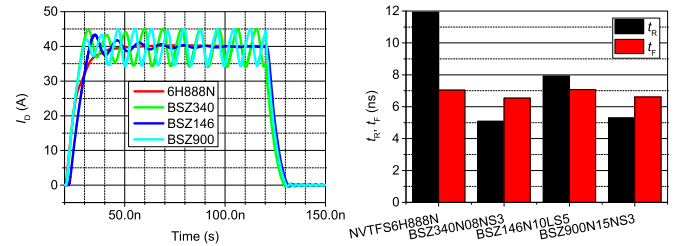
the edges were the best for these FETs. Edge durations for NVTFS6H888N were not the best, yet it did not cause the oscillations thanks to the lowest reverse capacitance (note C_R value in Table II). The boosted FET (NVTFS6H888N) source feedback topology was selected as the candidate.

It can be concluded that it is reasonable to expect rising and falling edges of 5–6 ns at 40-A pulsed current and a 40-V compliance voltage. It should be noted that the highest forward voltage laser diode was used in the simulation. Use of a lower forward voltage laser would give faster rise times.

Three topologies can satisfy the requirements for the generation of the APWP sets: a boosted resistor current limiter (Fig. 1, right), a constant current sink FET (Fig. 7), and an FET with source boost current feedback (Fig. 9).

E. Current Sensing

Current sensing is required to have feedback on the actual laser diode current. The most straightforward idea is to use a grounded current shunt resistor along a laser current path. While convenient for capacitor discharge (shunt resistor can be placed in series with D_{LD}, Fig. 4), such a solution is complicated for the constant current sink topologies: if a shunt resistor is placed in series with C_{HV}, then the charging current of this capacitor is also measured. Another solution would be to place a shunt at the high side and measure the differential voltage using a small signal transformer (Fig. 12, left).

A standard small signal transformer would suffice, such as for example, the CX2041 from Pulse Engineering, Inc. It has dimensions of 3.8 × 3.8 mm, has a 200-μH magnetizing inductance L_m, and so lower cutoff frequency of 400 Hz with an R_{SH} of 500 mΩ. If R_{SH} is located near C_{HV}, there is no influence from parasitic inter-winding capacitance. It is also possible to replace the transformer by a capacitor (as per the middle circuit in Fig. 12).

The main disadvantage with this sensing circuit is that low R_{SH} values are preferred, to keep the compliance voltage and
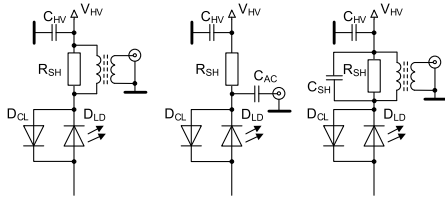
Fig. 12. High side current shunt using transformer (left), capacitor (center) and boosted shunt to reduce parasitic L effects (right) current sensing.
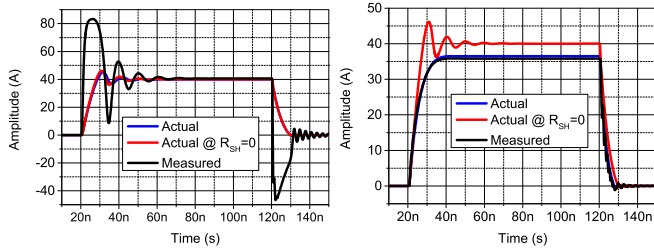

Fig. 13. Current sensing waveform of 50-mΩ shunt (left) and 500-mΩ shunt (right) comparison to actual current for FET current sink topology.
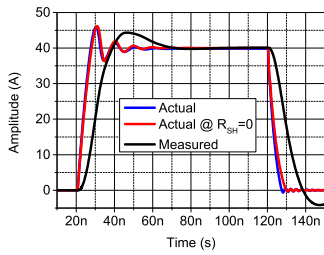

Fig. 14. Current sensing waveform of 100-mΩ shunt tampered by 100 nF: comparison to actual current for FET current sink topology using EPC2019.

efficiency high. In such a case, the parasitic inductance of R_{SH} might distort the measurement results by giving overshoots at edges. This is seen in the LT SPICE simulation results on the left in Fig. 13, for 50 mΩ and 0.6-nH parasitic inductance (three parallel standard wrap-around 0603 components) in Fig. 13, for an FET current sink topology using EPC2019. Thanks to the low R_{SH} value, the current flowing through the laser did not change significantly (compare red and blue curves), yet the current sensing signal derived on the shunt has peaks and oscillations (black curve).

If the R_{SH} value is increased, e.g., up to 0.5 Ω, even switching oscillations disappear, but the rising edge time increases significantly, from 5 to 10 ns (Fig. 13, right). Because of the higher R_{SH} value, the compliance voltage present on the laser is reduced by 20 V (0.5 Ω, 40 A). This causes not just the rise time reduction [refer (1)], but also a decrease of the set current, since the current feedback has a limited gain (compare the red and blue curves: 36 A versus 40 A). The resistor current limiter topology already has R_{SH} (actually it is R_{LIM}) and its value is as required, 0.5 Ω, so that it can use this current sensing circuitry without any modifications. Acceptable results (Fig. 14) can be achieved if R_{SH} is tampered by parallel capacitance (as per Fig. 12, right) and R_{SH} is slightly increased to 100 mΩ.
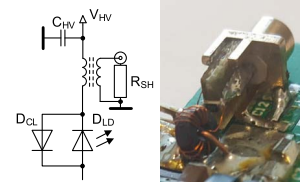
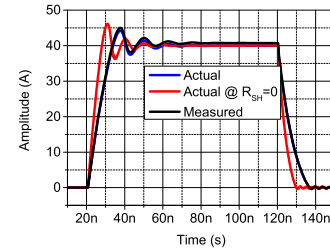Fig. 15. High side current sensing using current transformer.

Fig. 16. Current sensing waveform when using 1:10 current transformer: comparison to actual current for FET current sink topology using EPC2019.

Positive effect can also be noted on slightly improved edges (compare the blue and red curves). It should be noted that such a circuit corresponds to R_{FB} being used in an FET source feedback topology, so this topology also has inherent current sensing.

Another current sensing solution is a current transformer (Fig. 15). If R_{SH} is low and the transformer turns ratio n is high then resistance appearing on the primary is lower by n^2. Even a small toroidal core can be used. In the case presented here, a 3.8-mm diameter toroidal core, taken from a CX2052 transformer (Pulse Engineering, In., San Diego, CA, USA) was used. It has 1.6 μH per turn (A_L value), so a 1:10 turns ratio and 1 Ω R_{SH} would result in a 1-kHz lower cutoff frequency, which is more than enough for the target APWP signals.

A low resistance, transformed into the primary would result in low voltages, which in turn will prevent the core from saturation. Unfortunately, a high turns ratio reduces the coupling k, so that some leakage inductance remains, which might reduce the rising and falling edge speed of the laser driver. The inductance of the secondary winding of the transformer was measured at 1 MHz, giving $L_s = 377$ nH (primary shorted) and $L_2 = 168$ μH (primary open) values. The coupling factor k was calculated as 0.999 according to [101]

$$k = \sqrt{1 - \frac{L_s}{L_2}}. \tag{4}$$

Such a coupling factor would mean that there is a 1.8-nH leakage inductance present on the primary, which is a significant fraction of the estimated 4.6 nH of total current loop inductance. This situation was simulated using LT SPICE, and the results are presented in Fig. 16.

It is notable that the measured current (black curve) closely matches the actual laser current (blue curve), and rising and falling edges are reduced significantly: from 5 ns without current sensing transformer (red curve) to 10 ns with the transformer.
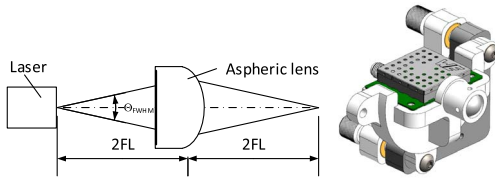
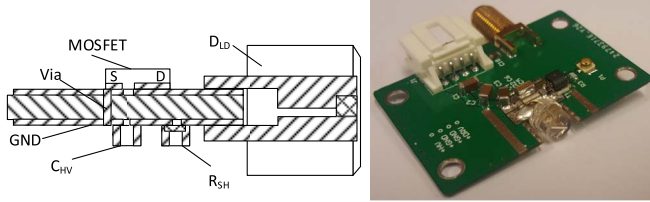Fig. 17. Optical system schematic (left) and assembled holder with kinematic mount 3-D drawing (right).

Fig. 18. Main current loop PCB cross section (left) and assembled PCB (right).

Fig. 19. Current transformer (left) and 100-mΩ shunt (right) current sensing.

Fig. 20. Photodetector schematic (left) and 3-D drawing of the assembled sensor (right).

F. Optical System

A simple optical system was used (Fig. 17), comprising one aspheric 10-mm diameter, 8.13-mm focal length (FL at 905 nm) lens ACL108U-B (Thorlabs Inc., Newton, NJ, USA) placed at the 2FL (16.4 mm) distance from the laser aperture.

Such a setup is compact and requires minimum adjustments and provides a magnification of 1:1, but at the expense of reduced beam coverage. For the largest fast axis beam divergence angle, 25° (refer Table I), the beam full width half power (FWHP) size, when entering the lens, is 5.1 mm.

The clear aperture of the lens (note thick line in Fig. 17, which is to scale) is more than 9 mm, so that less than 0.2% power loss is expected through the optics.

IV. Experimental Investigation Results

The output of the photodetector or preamplifier was digitized using a digital oscilloscope (Yokogawa DLM2054, 500-MHz bandwidth, equivalent to the 0.7-ns edge duration, 125 GS/s sampling rate with interpolation, Yokogawa Electric Corporation, Tokyo, Japan) when a single pulse or simple toneburst experiment was carried out. The laser system in these cases was driven by a Siglent SDG6022X arbitrary waveform generator (200-MHz bandwidth, 2.4 GS/s sampling rate, Siglent Technologies, Shenzhen, China).

A. Boosted MOSFET Source Current Feedback Laser Driver

The experimental investigation of the boosted Source current feedback topology (Fig. 9, right) using the NVTFS6H888N MOSFET is analyzed here. The current loop inductance reduction was achieved from the PCB layout. The main current loop was routed on a 0.6-mm thick substrate (Fig. 18).

The capacitor C_{HV} actually was constructed from a set of parallel connected 47-, 4.7-, and 0.47-μF capacitors, with the smallest in the main loop (Fig. 18) and the rest located away from the main loop. The distance from the MOSFET source to the PCB edge where the laser diode was soldered, was only 6 mm. The smallest capacitor $C_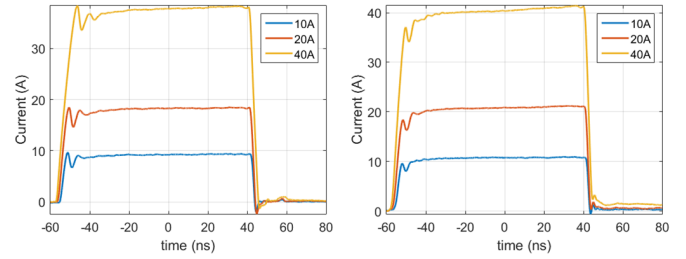{HV}$ and R_{SH} were of the inverse type 0612 size. The shunt resistor R_{SH} was a flipped type (resistive layer facing the PCB, note in Fig. 18, left) and the laser diode D_{LD} had minimal pin length, so that the loop area was significantly reduced. The whole PCB was 39 × 27 mm in size, with the essential components occupying an area of 10 × 20 mm (Fig. 18, right).
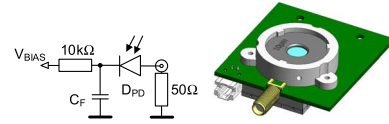
The current transformer better matches the laser current, as is seen in the comparison of current measured using current transformer (Fig. 19, left) and R_{FB} (used as R_{SH}) voltage (Fig. 19, right).

The setup for the optical output waveforms measurement is presented in Fig. 20. A fast (35-ps rise time) Si photodiode FDS015 (Thorlabs Inc., Newton, NJ, USA) was used, reverse biased with 5 V (Fig. 20, left). The diode has an active area of 150-μm diameter, which was further reduced by placing a 10-μm diameter pinhole on top of the diode (Fig. 20, right).

The current transformer has a slight detrimental effect on the switching speed (see Fig. 21: from 5.8 ns when no transformer is used to 7.2 ns with transformer at 40 A). Therefore, it was decided not to use current transformer for current sensing. All further experiments used the current shunt for laser current estimation. Laser driver current sensing was used to establish the required gate voltage and this voltage was used throughout succeeding experiments.

It is notable that there is some droop in optical output at 40 A. Explanation could be the laser efficiency reduction due to heating.

It should be noted that MOSFETs have larger reverse capacitance (C_{GD} = 3 pF, compare to 0.7 pF for GaN), therefore are sensitive to dV/dt effect when the fast falling drain voltage edge causes the MOSFET to turn off. Phenomenon can be mitigated by placing a small resistance in series with gate drive. Single-channel gate driver and 3-Ω gate resistor were used to reduce dV/dt turn-off effects. The waveforms presented above are for the nonboosted case. See Fig. 22 for the case when the filtering capacitor C_F is added in parallel to R_{FB}.

Pulses with widths down to 20 ns can be produced using the 20-nF boosted case (see Fig. 23) for a 20-ns pulse train with a 40-ns period. It is noted that current amplitude of pulses is the same for every programmed current (Fig. 23, right). Amplitude
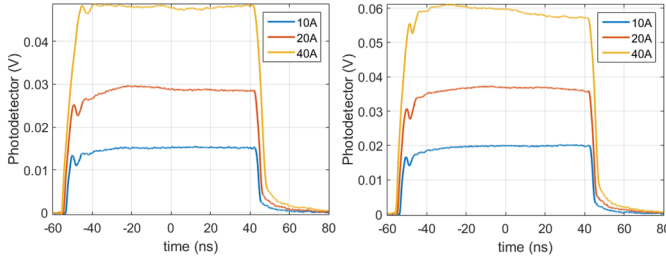
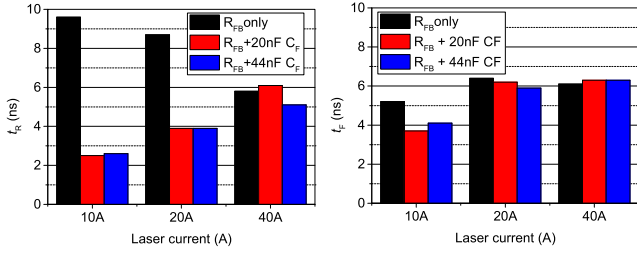Fig. 21.   Optical output with (left) and without (right) current transformer.

Fig. 24.   Current sensing waveform for 500-mΩ shunt in case of boosted resistor current limiter topology laser driver.

Fig. 22.   Measured rising (left) and falling (right) edges for boosted source feedback driver versus boost capacitance.
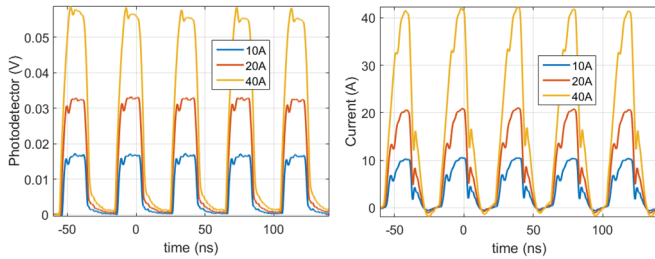

Fig. 25.   Optical output waveform (left) and speed (right) for boosted resistor current limiter driver.

Fig. 23.   Pulse train optical output (left) and current (right) for boosted source feedback topology.

Fig. 26.   Pulse train optical output (left) and current (right) for boosted resistor current limiter driver.

of pulses is dropping slightly (4%) at 40-A current. This can be explained by laser efficiency reduction due to heating.

It can be concluded that down to 20-ns pulse sets can be generated using NVTFS6H888N MOSFET in boosted source current feedback topology.

B. GaN Boosted Resistor Current Limiter Laser Driver

Experimental investigation of the boosted resistor current limiter (Fig. 1, right), using EPC2019 GaN FET driven by LMG1020 is analyzed in this section. The same approach as shown in Fig. 18 was used to minimize the current loop inductance, and the PCB was made from a 0.6-mm substrate. The current limiting resistance R_{LIM} was 500 mΩ, and the capacitance used for boosting the edge current, C_{BOOST} was 8 nF (which was located in the main loop as C_{HV} in Fig. 18). The same limiting resistor R_{LIM} was used as a current shunt (see the waveform obtained in Fig. 24).

The transition time looks slow because of the smoothing effect of the boosting capacitance, but the actual laser current so the optical output edges are steeper (refer Fig. 25).

The rise time is slower at low currents because of lower compliance voltage. Voltage V_{HV} had to be varied to get the
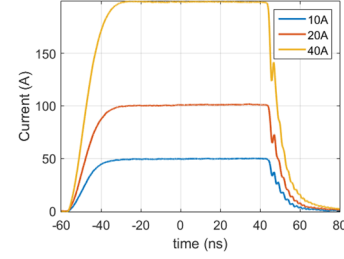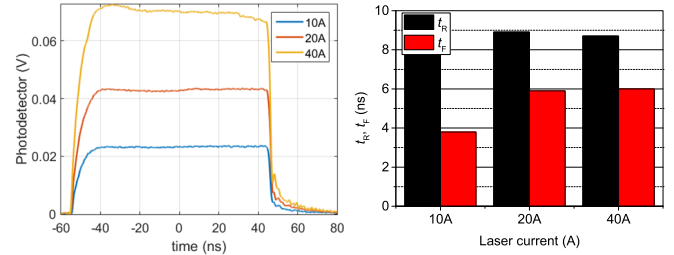
corresponding laser current (33 V for 40 A, 20 V for 20 A, and 12 V for 10 A).

Pulses as short as 20 ns can be produced, as is seen for the pulse train with 20-ns pulses with a 40-ns period in Fig. 26.

It can be noted that pulse amplitude is stable, only 40-A current has a 9% drop between last and first pulse. It is more pronounced than boosted source feedback (4%) because the laser heating and the current drop combine.

C. GaN Constant Current Sink Laser Driver

The experimental investigation of the constant current sink FET (Fig. 7) using the EPC2019 GaN FET is analyzed in this section. The same approach as for Fig. 18 was used to minimize the current loop inductance, and the PCB was made on 0.6-mm substrate. The current was measured using a 100-mΩR_{SH} as per Fig. 12 (right). The shunt resistance was tampered by the 20-nF capacitor to filter the oscillations caused by the parasitic inductance, and to provide some boost on the edges. The waveform recorded on R_{SH} is presented in Fig. 27.

It is noted that there is some peaking in the current, the same is registered on the optical output (Fig. 28, left). Measured edges of the optical output are presented in Fig. 28 (right).
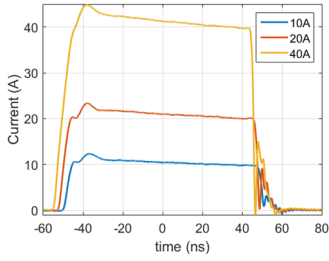
Fig. 27.   Current sensing waveform for 100-mΩ shunt for current sink driver.
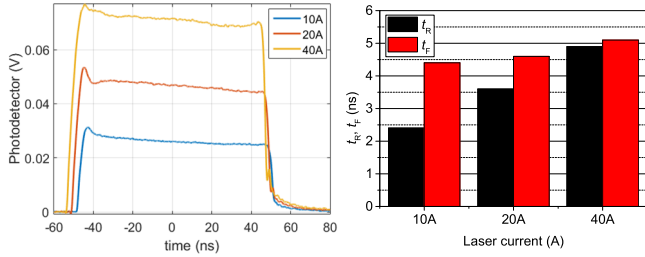

Fig. 28.   Optical output waveform (left) and speed (right) for constant current sink FET laser driver.
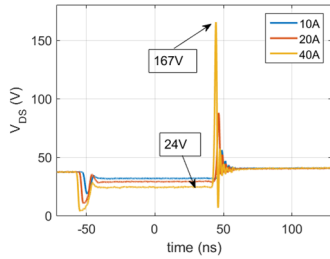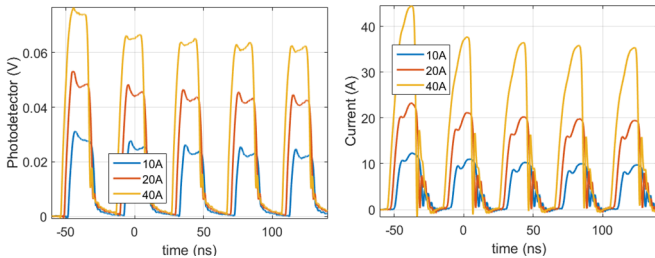

Fig. 29. V_{DS} voltage for constant current sink FET laser driver.

Fig. 30.   Pulse train optical output (left) and current (right) for constant current sink FET laser driver.

It is noted also, that there is a drop in the optical output and laser current (Fig. 27). The possible reason could be the heating of the constant current FET: all of the compliance voltage drop is on the FET, so that significant instant power is dissipated on the FET. The drain voltage according to Fig. 29 is 24 V, which corresponds to 960-W instantaneous power.

The clamping diode D_{CL} was placed close to the laser, to reduce the falling edge duration, the penalty for doing so being a 167-V drain voltage induced after FET turn off (which is still below the 200-V breakdown according Table I).

The waveform of the optical output in response to the pulse train (20-ns duration, 40-ns period) is presented in Fig. 30.

The pulse amplitude drop for this topology is the most visible, with the last pulse amplitude (62 mV) being 19% less than the first pulse amplitude (76 mV). The drop is present for both high and low driving currents.
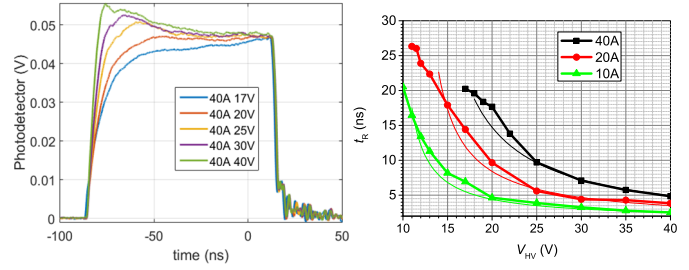

Fig. 31.   Optical output variation with different compliance voltages (left) and the attainable rising edge duration (right) versus compliance voltage for constant current sink FET laser driver.
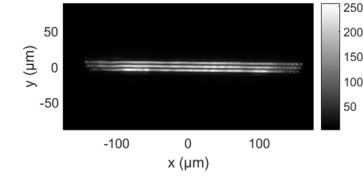

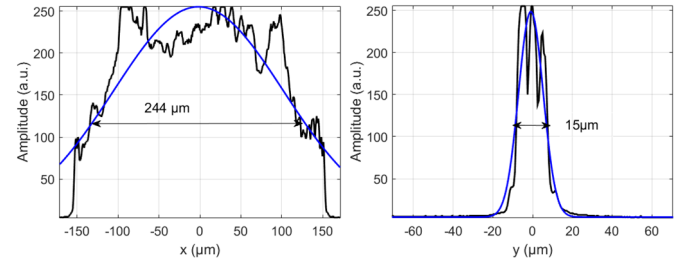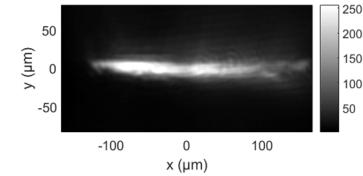Fig. 32.   2-D near-field beam profile.

Fig. 33.   Measured (black curve) and approximated (blue curve) near-field beam profile along *x*-axis (left) and *y*-axis (right).

Fig. 34.   2-D focused laser beam profile.

It is possible to program the rising edge duration by changing the V_{HV} voltage, and adjusting the gate drive voltage. See the signals obtained in Fig. 31, left (gate voltage was adjusted to maintain a current of 40 A). The attainable rising edge duration versus the compliance voltage is presented in Fig. 31 (right). The thin lines are theoretical estimates, derived from (1)

$$t_R = \frac{I_{LD} \cdot L}{V_{HV} - V_{LD}} + t_{drv} \qquad (5)$$

where I_{LD} is the laser diode current, V_{LD} is the laser forward voltage (can be obtained from Fig. 29), t_{drv} is the additional delay from gate driver, and L is the main current loop inductance. The main current loop inductance (3.2 nH) was estimated by fitting (5) to Fig. 31 results.

The GaN constant current sink FET topology was used in further measurements.

D. Beam Profile

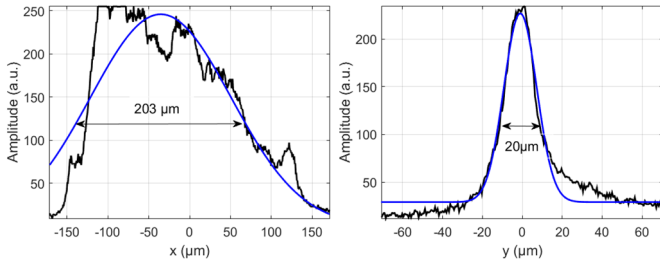Beam profile was measured using the 1280 × 1024 pixels monochromatic CMOS camera [102] and 1:4 beam expander.

Fig. 35. Focused laser beam profile along *x*-axis (left) and *y*-axis (right): measured (black) and approximated (blue).
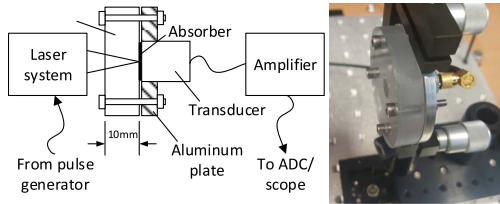

Fig. 36. Setup for photoacoustic response measurement diagram (left) and photo of the assembled clear PC disk with transducer (right).
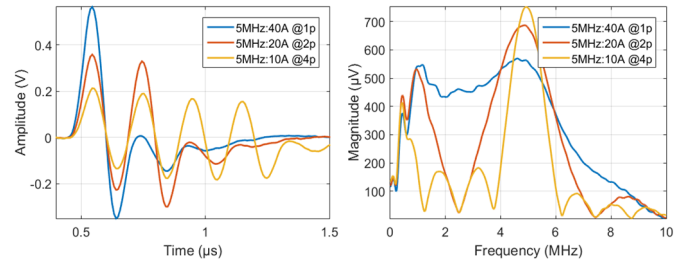

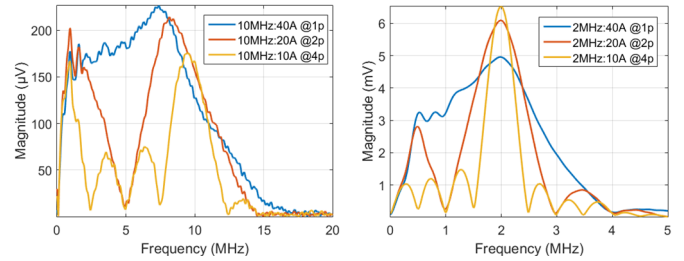Fig. 37. Photoacoustic response in time (left) and frequency (right) domain for 5-MHz transducer.

Fig. 38. Photoacoustic response spectrum for 10 MHz (left) and 2 MHz (right) transducer after propagation through 10-mm PEEK.

A pixel pitch of 5.07 μm was estimated using an optical calibration scale. The beam profile images obtained (Figs. 32 and 34) were used for beamwidth measurements. A slice of the measured profile (black curves) along the *x*-axis (parallel to the junction, slow axis, Figs. 33 and 35, left) or along the *y*-axis (fast axis, Figs. 33 and 35, right) was approximated (blue curves) by a Gaussian function with a dc offset [103] to extract the FWHP beam size.

It was found that the beam spot was subject to comma and other off-axis defects, since there was no laser beam nor lens alignment. This can be seen by comparing the near-field beam profile (Figs. 32 and 33) to focal spot images in Figs. 34 and 35.

It should be noted that asymmetric beam profile might influence the produced acoustic output directivity: such a beam profile is equivalent to line source excitation [22], [74], [104]–[106]. If the surface is not constrained, the Rayleigh surface waves will dominate. This property can be attractive in applications where surface defects have to be detected [16], [35], [105]. In this article, the target is the longitudinal wave generation (propagating normal to the surface). Fortunately, in the case of the constrained acoustic source, the amplitude of the longitudinal waves is significantly enhanced [44].

E. Acoustic Output

The photoacoustic response was measured using the ultrasonic transducer with its receiving surface exposed to the focused laser beam (Fig. 36). The surface of the transducer was coated by an absorbing coating (black permanent marker, Stanley, Fine Tip). The transducer was screwed into a 4-mm thick aluminum plate, which in turn was bolted to a 10-mm thick clear polycarbonate (PC) disk. The PC disk served as a constraining layer to increase the longitudinal wave amplitude directed normal to the surface [38]–[45].

Three thread-in, contact type 6-mm active element diameter transducers were used: a 2-MHz C542-SM, a 5-MHz

C543-SM, and a 10-MHz C544-SM (Olympus Corp., Westborough, MA, USA). The transducers were of the CENTRASCAN design, which offers both high sensitivity and wide bandwidth. The transducer output was fed into the wideband (0.5–30-MHz range) programmable gain (7–47-dB range) preamplifier [107].

An example of the acoustic output for the 5-MHz ultrasonic transducer for different pulse duration (1, 2, and 4 periods) and amplitude (10 A for four periods to 40 A for one pulse) toneburst signal and its spectrum are presented in Fig. 37.

The response for 2- and 10-MHz transducer when a 10-mm PEEK (polyetheretherketone) was inserted between PC and transducer is presented in Fig. 38.

The attenuation effects can be seen in Fig. 38, left: the high frequency components have been attenuated while propagating in plastic. The experiments reported above demonstrate that the signal frequency content can be concentrated in the band of interest, when using a pulse sequence. Meanwhile, a single pulse has a lot of energy concentrated close to dc, which is of little use for ultrasonic measurements.

A dedicated ultrasonic signals acquisition system was used both to drive the laser system (binary code sets at 100-MHz sampling rate) and to digitize the preamplifier output (10 bit, 100-MHz sampling rate) [107], when generation of the complex APWP sequences was required.

A demonstration of the more complex APWP SS [108], [109] waveforms (at 10-A current, when using the SPL-PL90-3 laser) for a 5-MHz transducer surface probing is presented in Fig. 39 (one period chip PSK signal coded by 13 elements Barker code) and Fig. 40 (6.5-μs duration chirp with 10–3-MHz frequency sweep).

It can be seen that amplitude of the signal is increased (compared to a single-pulse response in Fig. 41).

The experiments above have been carried out at current of 10 A, because safe operation area of the laser does not permit
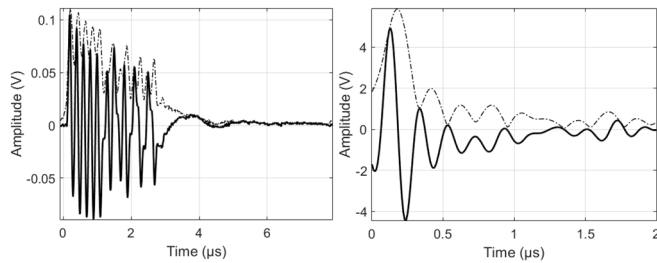
Fig. 39. Raw (left) and compressed (right) output for 5-MHz transducer excited by PSK signal coded by 13 elements Barker code (dashed line – envelope).
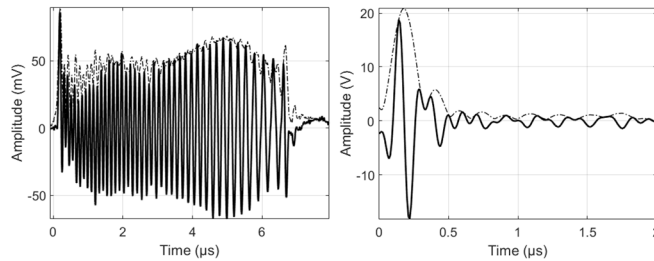

Fig. 40. Raw (left) and compressed (right) output for 5-MHz transducer excited by chirp with 10- to 3-MHz frequency sweep (dashed line – envelope).
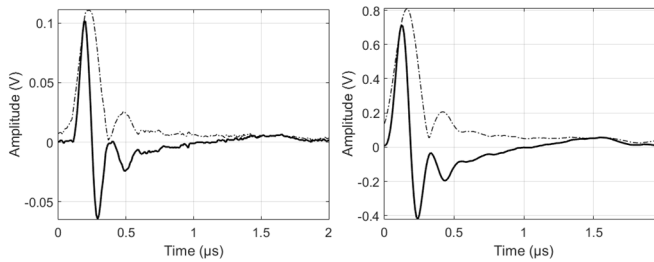

Fig. 41. Raw (left) and compressed (right) output for 5-MHz transducer excited by a single pulse (dashed line – envelope).

one to use such long pulse sets. Higher currents can be used with the new generations of laser diode that are now available.

V. CONCLUSION

A compact driver for laser ultrasonics experiments with APWP sequences has been developed. While it was concluded that GaN-based constant current switch topology has best performance, power MOSFET in source current feedback topology has a comparable performance. Latter topology produces more stable amplitude. Both topologies can supply up to 40-A pulse sets, where individual pulse duration can vary between 20 and 1000 ns, which allows one to cover frequencies in the 0.5–25-MHz ultrasound range. Shorter pulse durations can be attained, but at durations below 10 ns the pulse amplitude decreases. Longer pulse durations beyond 1000 ns can be used, but there is some output decrease beyond this point due to FET and laser heating. It has been demonstrated that the acoustic outputs for 2-, 5-, and 10-MHz transducers can be programmed, by changing the spectral content of the excitation signal via complex SS signals (PSK or chirp). The further development could be concentrated on the photoacoustic output and directivity, in relation to the optical system and excitation set design studies.

REFERENCES

[1] O. Couture, V. Hingot, B. Heiles, P. Muleki-Seya, and M. Tanter, "Ultrasound localization microscopy and super-resolution: A state of the art," *IEEE Trans. Ultrason., Ferroelectr., Freq. Control*, vol. 65, no. 8, pp. 1304–1320, Aug. 2018, doi: 10.1109/TUFFC.2018.2850811.

[2] H. Huang and D. Paramo, "Broadband electrical impedance matching for piezoelectric ultrasound transducers," *IEEE Trans. Ultrason., Ferroelectr., Freq. Control*, vol. 58, no. 12, pp. 2699–2707, Dec. 2011, doi: 10.1109/TUFFC.2011.2132.

[3] T. Misaridis and J. A. Jensen, "Use of modulated excitation signals in medical ultrasound. Part II: Design and performance for medical imaging applications," *IEEE Trans. Ultrason., Ferroelectr., Freq. Control*, vol. 52, no. 2, pp. 192–207, Feb. 2005, doi: 10.1109/TUFFC.2005.1406546.

[4] S. Kageyama, H. Hasegawa, and H. Kanai, "Increasing bandwidth of ultrasound radio frequency echoes using Wiener filter for improvement of accuracy in measurement of intima-media thickness," *Jpn. J. Appl. Phys.*, vol. 52, no. 7, pp. 07HF04-1–07HF04-6, Jul. 2013, doi: 10.7567/JJAP.52.07HF04.

[5] S. Dixon, C. Edwards, and S. B. Palmer, "High accuracy non-contact ultrasonic thickness gauging of aluminium sheet using electromagnetic acoustic transducers," *Ultrasonics*, vol. 39, no. 6, pp. 445–453, 2001.

[6] J. Shin, Y. Chen, H. Malhi, and J. T. Yen, "Ultrasonic reverberation clutter suppression using multiphase apodization with cross correlation," *IEEE Trans. Ultrason., Ferroelectr., Freq. Control*, vol. 63, no. 11, pp. 1947–1956, Nov. 2016, doi: 10.1109/TUFFC.2016.2597124.

[7] A. S. Savoia, M. La Mura, B. Mauti, N. Lamberti, and G. Caliano, "Reverberation reduction in capacitive micromachined ultrasonic transducers (CMUTs) by front-face reflectivity minimization," *Phys. Proc.*, vol. 70, pp. 941–944, Jan. 2015, doi: 10.1016/j.phpro.2015.08.195.

[8] R. M. White, "Generation of elastic waves by transient surface heating," *J. Appl. Phys.*, vol. 34, no. 12, pp. 3559–3567, Dec. 1963, doi: 10.1063/1.1729258.

[9] S. J. Davies, C. Edwards, G. S. Taylor, and S. B. Palmer, "Laser-generated ultrasound: Its properties, mechanisms and multifarious applications," *J. Phys. D, Appl. Phys.*, vol. 26, no. 3, pp. 329–348, Mar. 1993, doi: 10.1088/0022-3727/26/3/001.

[10] J. P. Monchalin, "Laser-ultrasonics: Principles and industrial applications," *E-J. Nondestruct. Test.*, vol. 3, pp. 1–43, Jun. 2020.

[11] J. P. Monchalin, "Progress towards the application of laser-ultrasonics in industry," in *Proc. QNDE*, vol. 12, 1993, pp. 495–506.

[12] C. B. Scruby, and L. E. Drain, *Laser-Ultrasonics: Techniques and Applications*. Bristol, U.K.: Adam Hilger, 1990.

[13] D. Royer, M. H. Noroy, and M. Fink, "Optical generation and detection of elastic waves in solids," *J. Phys.*, vol. 4, no. 7, pp. 673–684, 1994, doi: 10.1051/jp4:19947159.jpa-00253218.

[14] K. C. Kang, Y. H. Kim, W. Y. Choi, and K. K. Park, "Measurement of shallow defects using noncontact broadband leaky Lamb wave produced by pulsed laser with ultrasound microphone," *NDT E Int.*, vol. 111, Apr. 2020, Art. no. 102224, doi: 10.1016/j.ndteint.2020.102224.

[15] A. D. Friedman, "Theoretical and experimental study of generation mechanisms for laser ultrasound in woven graphite/epoxy composites with translaminar stitching," Ph.D. dissertation, Dept. Appl. Sci., College William & Mary-Arts & Sci., Williamsburg, VA, USA, 2000.

[16] A. M. Aindow, R. J. Dewhurst, and S. B. Palmer, "Laser generation of directional surface acoustic wave pulses in metals," *Opt. Commun.*, vol. 42, no. 116, pp. 116–120,1982, doi: 10.1016/0030-4018(82)90378-9.

[17] X. Wang *et al.*, "Focused bulk ultrasonic waves generated by ring-shaped laser illumination and application to flaw detection," *J. Appl. Phys.*, vol. 80, no. 8, pp. 4274–4281, Oct. 1996, doi: 10.1063/1.363387.

[18] S. Dixon, T. Harrison, Y. Fan, and P. A. Petcher, "Thermoelastic laser generated ultrasound using a ring source," *J. Phys. D, Appl. Phys.*, vol. 45, no. 17, May 2012, Art. no. 175103, doi: 10.1088/0022-3727/45/17/175103.

[19] D. Yi, C. Pei, T. Liu, and Z. Chen, "Inspection of cracks with focused angle beam laser ultrasonic wave," *Appl. Acoust.*, vol. 145, pp. 1–6, Feb. 2019, doi: 10.1016/j.apacoust.2018.09.012.

[20] J. Guan, Z. Shen, X. Ni, J. Lu, J. Wang, and B. Xu, "Numerical simulation of the ultrasonic waves generated by ring-shaped laser illumination patterns," *Opt. Laser Technol.*, vol. 39, no. 6, pp. 1281–1287, Sep. 2007, doi: 10.1016/j.optlastec.2006.07.007.

[21] D. Cerniglia, A. Pantano, and C. Mineo, "Influence of laser beam profile on the generation of ultrasonic waves," *Appl. Phys. A, Solids Surf.*, vol. 105, pp. 959–967, Oct. 2011, doi: 10.1007/s00339-011-6520-z.

[22] V. V. Krylov, "Directivity patterns of laser-generated sound in solids: Effects of optical and thermal parameters," *Ultrasonics*, vol. 69, pp. 279–284, Jul. 2016.

[23] J. M. S. Sakamoto, B. R. Tittmann, A. Baba, and G. M. Pacheco, "Directivity measurements in aluminum using a laser ultrasonics system," *J. Phys. Ser.*, vol. 278, Oct. 2011, Art. no. 012032, doi: 10.1088/1742-6596/278/1/012032.

[24] A. G. Every, Z. N. Utegulov, and I. A. Veres, "Laser thermoelastic generation in metals above the melt threshold," *J. Appl. Phys.*, vol. 114, no. 20, Nov. 2013, Art. no. 203508, doi: 10.1063/1.4832483.

[25] A. M. Aindow, R. J. Dewhurst, D. A. Hutchins, and S. B. Palmer, "Laser-generated ultrasonic pulses at free metal surfaces," *J. Acoust. Soc. Amer.*, vol. 69, no. 2, pp. 449–455, 1981.

[26] C. B. Scruby, R. J. Dewhurst, D. A. Hutchins, and S. B. Palmer, "Laser generation of ultrasound in metals," *Res. Techn. Nondestruct. Test.*, vol. 5, no. 8, pp. 281–327, 1982.

[27] L. F. Bresse and D. A. Hutchins, "Transient generation by a wide thermoelastic source at a solid surface," *J. Appl. Phys.*, vol. 65, pp. 1441–1449, Feb. 1989, doi: 10.1063/1.342956.

[28] C. B. Scruby, H. N. G. Wadley, R. J. Dewhurst, S. B. Palmer, and D. A. Hutchins, "A laser-generated standard acoustic emission source," *Mater. Eval.*, vol. 39, pp. 1250–1254, Dec. 1981.

[29] J. Laloš, M. Jezeršek, and T. Požar, "Laser-induced ultrasonic waveform derivation and transition from a point to a homogeneous illumination of a plate," *Ultrasonics*, vol. 81, pp. 158–166, Nov. 2017.

[30] I. G. Calasso, W. Craig, and G. J. Diebold, "Photoacoustic point source," *Phys. Rev. Lett.*, vol. 86, no. 16, pp. 3550–3553, May 2001.

[31] K. Zhang, G. Lv, S. Guo, D. Chen, Y. Liu, and W. Feng, "Evaluation of subsurface defects in metallic structures using laser ultrasonic technique and genetic algorithm-back propagation neural network," *NDT E Int.*, vol. 116, Dec. 2020, Art. no. 102339, doi: 10.1016/j.ndteint.2020.102339.

[32] C.-H. Yang, N. Jeyaprakash, and C.-K. Chan, "Inhomogeneous mechanical properties in additively manufactured parts characterized by nondestructive laser ultrasound technique," *NDT E Int.*, vol. 116, Dec. 2020, Art. no. 102340, doi: 10.1016/j.ndteint.2020.102340.

[33] J. Yang and I. C. Ume, "Laser ultrasonic technique for evaluating solder bump defects in flip chip packages using modal and signal analysis methods," *IEEE Trans. Ultrason., Ferroelectr., Freq. Control*, vol. 57, no. 4, pp. 920–932, Apr. 2010, doi: 10.1109/TUFFC.2010.1496.

[34] S. G. Pierce and B. Culshaw, "Laser generation of ultrasonic Lamb waves using low power optical sources," *IEE Proc.-Sci., Meas. Technol.*, vol. 145, no. 5, pp. 244–249, Sep. 1998, doi: 10.1049/ip-smt:19982212.

[35] N. Montinaro, G. Epasto, D. Cerniglia, and E. Guglielmino, "Laser ultrasonics for defect evaluation on coated railway axles," *NDT E Int.*, vol. 116, Dec. 2020, Art. no. 102321, doi: 10.1016/j.ndteint.2020.102321.

[36] D. A. Hutchins, R. J. Dewhurst, and S. B. Palmer, "Laser generated ultrasound at modified metal surfaces," *Ultrasonics*, vol. 19, no. 3, pp. 103–108, May 1981.

[37] V. V. Shah, K. Balasubramaniam, and J. P. Singh, "Effect of surface coatings on generation of laser based ultrasound," in *Proc QNDE*, vol. 14, 1995, pp. 569–576.

[38] E. Biagi, F. Margheri, and D. Menichelli, "Efficient laser-ultrasound generation by using heavily absorbing films as targets," *IEEE Trans. Ultrason., Ferroelectr., Freq. Control*, vol. 48, no. 6, pp. 1669–1680, Feb. 2001.

[39] T. Buma, M. Spisar, and M. O'Donnell, "High-frequency ultrasound array element using thermoelastic expansion in an elastomeric film," *Appl. Phys. Lett.*, vol. 79, no. 4, pp. 548–550, Jul. 2001, doi: 10.1063/1.1388027.

[40] C. Edwards, T. Stratoudaki, and S. B. Palmer, "A new thermoelastic source model for non-metals," in *Proc. QNDE*, vol. 22, 2003, pp. 326–332.

[41] F. Gao *et al.*, "An analytical study of photoacoustic and thermoacoustic generation efficiency towards contrast agent and film design optimization," *Photoacoustics*, vol. 7, pp. 1–11, Sep. 2017.

[42] S. M. Nikitin *et al.*, "Directivity patterns and pulse profiles of ultrasound emitted by laser action on interface between transparent and opaque solids: Analytical theory," *J. Appl. Phys.*, vol. 115, no. 4, Jan. 2014, Art. no. 044902, doi: 10.1063/1.4861882.

[43] J. A. Guggenheim, E. Z. Zhang, and P. C. Beard, "A method for measuring the directional response of ultrasound receivers in the range 0.3–80 MHz using a laser-generated ultrasound source," *IEEE Trans. Ultrason., Ferroelectr., Freq. Control*, vol. 64, no. 12, pp. 1857–1863, Dec. 2017.

[44] J. B. Spicer, F. W. Zeng, and L. R. Olasov, "Subsurface, thermoelastic line source excitation of a transversely isotropic half space," *Wave Motion*, vol. 72, pp. 87–100, Jul. 2017, doi: 10.1016/j.wavemoti.2016.12.004.

[45] J. Wang, B. Xu, Z. Shen, X. Ni, and J. Lu, "Influence of transparent coating thickness on thermoelastic force source and laser-generated ultrasound waves," *Appl. Surf. Sci.*, vol. 255, no. 16, pp. 7172–7178, May 2009, doi: 10.1016/j.apsusc.2009.03.054.

[46] A. Kathryn, C. Brian, D. Fengzhong, J. Pan, G. Pierce, and C. Swift, "Generation and detection of broadband laser generated ultrasound from low-power laser sources," *Proc. SPIE*, vol. 4417, pp. 19–32, Sep. 2001, doi: 10.1117/12.441302.

[47] I. A. Veres *et al.*, "Golay code modulation in low-power laser-ultrasound," *Ultrasonics*, vol. 53, no. 1, pp. 122–129, Jan. 2013, doi: 10.1016/j.ultras.2012.04.006.

[48] S. G. Pierce *et al.*, "Low peak-power laser ultrasonics," *Nondestruct. Test. Eval.*, vol. 26, nos. 3–4, pp. 281–301, Sep. 2011, doi: 10.1080/10589759.2011.573549.

[49] R. F. Anastasi and E. I. Madaras, "Pulse compression techniques for laser generated ultrasound," in *Proc. IEEE IUS*, vol. 1, Oct. 1999, pp. 813–817, doi: 10.1109/ULTSYM.1999.849521.

[50] D. Vangi, A. Virga, and M. S. Gulino, "Random sequence for optimal low-power laser generated ultrasound," *J. Phys. Conf. Ser.*, vol. 882, Jun. 2017, Art. no. 012013, doi: 10.1088/1742-6596/882/1/012013.

[51] D. Vangi, A. Virga, and M. Gulino, "Study on the most influential parameters in low-power laser generated ultrasound," *FME Trans.*, vol. 45, no. 3, pp. 323–330, 2017, doi: 10.5937/fmet1703323V.

[52] D. Vangi, M. S. Gulino, and A. Virga, "Optimal Rayleigh waves generation by continuous wave modulated laser," *J. Phys., Conf. Ser.*, vol. 1110, Oct. 2018, Art. no. 012006, doi: 10.1088/1742-6596/1110/1/012006.

[53] C. Canal, A. Laugustin, A. Kohl, and O. Rabot, "Portable multiwavelength laser diode source for handheld photoacoustic devices," *Proc. SPIE*, vol. 9887, Apr. 2016, Art. no. 98872B, doi: 10.1117/12.2227107.

[54] T. H. Wang, S. Nandy, H. S. Salehi, P. D. Kumavor, and Q. Zhu, "A low-cost photoacoustic microscopy system with a laser diode excitation," *Biomed. Opt. Exp.*, vol. 5, no. 9, pp. 3053–3058, Sep. 2014, doi: 10.1364/BOE.5.003053.

[55] M. Erfanzadeh and Q. Zhu, "Low-cost laser scanning photoacoustic microscopy system with a pulsed laser diode excitation source," *Proc. SPIE*, vol. 10064, Mar. 2017, Art. no. 100644R, doi: 10.1117/12.2249618.

[56] A. Hariri *et al.*, "Development of low-cost photoacoustic imaging systems using very low-energy pulsed laser diodes," *J. Biomed. Opt.*, vol. 22, no. 7, Jul. 2017, Art. no. 075001, doi: 10.1117/1.JBO.22.7.075001.

[57] P. K. Upputuri and M. Pramanik, "Fast photoacoustic imaging systems using pulsed laser diodes: A review," *Biomed. Eng. Lett.*, vol. 8, no. 2, pp. 167–181, May 2018, doi: 10.1007/s13534-018-0060-9.

[58] M. Erfanzadeh, H. S. Salehi, P. Kumavor, and Q. Zhu, "Improvement and evaluation of a low-cost laser diode photoacoustic microscopy system for ovarian tissue imaging," *Proc. SPIE*, vol. 9708, Mar. 2016, Art. no. 97083I, doi: 10.1117/12.2208943.

[59] M. Erfanzadeh, P. D. Kumavor, and Q. Zhu, "Laser scanning laser diode photoacoustic microscopy system," *Photoacoustics*, vol. 9, pp. 1–9, Mar. 2018, doi: 10.1016/j.pacs.2017.10.001.

[60] R. Manwar, M. Hosseinzadeh, A. Hariri, K. Kratkiewicz, S. Noei, and M. N. Avanaki, "Photoacoustic signal enhancement: Towards utilization of low energy laser diodes in real-time photoacoustic imaging," *Sensors*, vol. 18, no. 10, p. 3498, Oct. 2018, doi: 10.3390/s18103498.

[61] M. Erfanzadeh and Q. Zhu, "Photoacoustic imaging with low-cost sources; a review," *Photoacoustics*, vol. 14, pp. 1–11, Jun. 2019, doi: 10.1016/j.pacs.2019.01.004.

[62] L. Zeng, G. Liu, D. Yang, and X. Ji, "Portable optical-resolution photoacoustic microscopy with a pulsed laser diode excitation," *Appl. Phys. Lett.*, vol. 102, no. 5, Feb. 2013, Art. no. 053704, doi: 10.1063/1.4791566.

[63] A. Cebrecos, J. J. Garcia-Garrigos, A. Descals, J. M. Benlloch, and F. Camarena, "Beamforming for large-area scan and improved SNR in array-based photoacoustic microscopy," *Ultrasonics*, vol. 111, Mar. 2021, Art. no. 106317, doi: 10.1016/j.ultras.2020.106317.

[64] M. N. Cherkashin, C. Brenner, and M. R. Hofmann, "Transducer-matched multipulse excitation for signal-to-noise ratio improvement in diode laser-based photoacoustic systems," *J. Biomed. Opt.*, vol. 24, no. 4, p. 1, Apr. 2019, doi: 10.1117/1.JBO.24.4.046001.

[65] A. Blouin, D. Levesque, C. Neron, D. Drolet, and J. P. Monchalin, "Improved resolution and signal-to-noise ratio in laser-ultrasonics by SAFT processing," *Opt. Exp.*, vol. 2, no. 13, pp. 531–539, Jun. 1998, doi: 10.1364/OE.2.000531.

[66] W. He *et al.*, "Study on the detection ability of laser ultrasonic SAFT technology for lead internal defects," *Proc. SPIE*, vol. 11717, Dec. 2020, Art. no. 117173B, doi: 10.1117/12.2587582.

[67] H. K. Zhang, M. A. L. Bell, X. Guo, H. J. Kang, and E. M. Boctor, "Synthetic-aperture based photoacoustic re-beamforming (SPARE) approach using beamformed ultrasound data," *Biomed. Opt. Exp.*, vol. 7, no. 8, p. 3056, Aug. 2016, doi: 10.1364/BOE.7.003056.

[68] J. R. Fincke, C. M. Wynn, R. Haupt, X. Zhang, D. Rivera, and B. Anthony, "Characterization of laser ultrasound source signals in biological tissues for imaging applications," *J. Biomed. Opt.*, vol. 24, no. 2, p. 1, Dec. 2018, doi: 10.1117/1.JBO.24.2.021206.

[69] L. Svilainis and A. Aleksandrovas, "Application of arbitrary pulse width and position trains for the correlation sidelobes reduction for narrowband transducers," *Ultrasonics*, vol. 53, pp. 1344–1348, Sep. 2013.

[70] L. Svilainis, A. Chaziachmetovas, D. Kybartas, and T. G. Alvarez-Arenas, "Air-coupled ultrasonic probe integrity test using a focused transducer with similar frequency and limited aperture for contrast enhancement," *Sensors*, vol. 20, no. 24, p. 7196, Dec. 2020, doi: 10.3390/s20247196.

[71] J. Storpellinen, M. Oksanen, R. Vuohelainen, J. Rantala, J. Hartikainen, and M. Luukkala, "Photoacoustic inspection of matching layers of ultrasonic air-coupled transducers," in *Proc. IEEE IUS*, vols. 1–2, Oct. 1989, pp. 665–668.

[72] L. Svilainis, D. Kybartas, A. Aleksandrovas, and T. E. G. Alvarez-Arenas, "High frequency focused imaging for ultrasonic probe integrity inspection," *NDT E Int.*, vol. 116, Dec. 2020, Art. no. 102360, doi: 10.1016/j.ndteint.2020.102360.

[73] L. Svilainis, A. Rodriguez-Martinez, A. Chaziachmetovas, and A. Aleksandrovas, "Ultrasound transmission spectral compensation using arbitrary position and width pulse sets," *IEEE Trans. Instrum. Meas.*, vol. 67, no. 8, pp. 1778–1785, Aug. 2018, doi: 10.1109/TIM.2018.2809838.

[74] A. Aharoni, K. M. Jassby, and M. Tur, "The thermoelastic surface strip source for laser-generated ultrasound," *J. Acoust. Soc. Amer.*, vol. 92, no. 6, pp. 3249–3258, Dec. 1992, doi: 10.1121/1.404175.

[75] *NTTFS4985NF MOSFET—Power, Single, N-Channel, WDFN8 30V, 64A*, ON Semiconductor, Phoenix, AZ, USA, 2019.

[76] J. Nissinen and J. Kostamovaara, "A 4 a peak current and 2 ns pulse width CMOS laser diode driver for high measurement rate applications," in *Proc. ESSCIRC*, Oct. 2013, pp. 355–358, doi: 10.1109/ESSCIRC.2013.6649146.

[77] M. Morgan, "Development of a novel time-of-flight laser rangefinder for opto-mechatronic applications," M.S. thesis, Dept. Eng. Appl. Sci., Memorial Univ. Newfoundland, St. John's, NL, Canada, May 2020.

[78] *Nanosecond Laser Driver Reference Design for LiDAR*, Texas Instruments, Dallas, TX, USA, 2018.

[79] H. W. Ott, *Electromagnetic Compatibility Engineering*. Hoboken, NJ, USA: Wiley, 2009.

[80] J. S. Glaser, "eGaN FETs for lidar—Getting the most out of the EPC9126 laser driver," EPC, Vellore, India, Tech. Rep. AN027, 2020, pp. 1–11.

[81] J. Cain, "Parasitic inductance of multilayer ceramic capacitors," AVX Corp., Fountain, SC, USA, Tech. Rep., 2020.

[82] *Frequency Response of Thin Film Chip Resistors*, Vishay Electronic GmbH, Mathur, India, Feb. 2009.

[83] D. Hodgson, K. Noonan, B. Olsen, and T. Orosz, "Pulsing a laser diode," ILX Lightw. Corp., Bozeman, MT, USA, Tech. Rep. Rev01.122804, 2004.

[84] L. Hallman, J. Huikari, and J. Kostamovaara, "A high-speed/power laser transmitter for single photon imaging applications," in *Proc. IEEE Sensors*, Nov. 2014, pp. 1–4.

[85] A. Liero, A. Klehr, T. Hoffmann, T. Prziwarka, and W. Heinrich, "GaN laser driver switching 30 a in the sub-nanosecond range," in *Proc. EUMIC*, 2016, pp. 460–463.

[86] T. J. Allen and P. C. Beard, "Pulsed near-infrared laser diode excitation system for biomedical photoacoustic imaging," *Opt. Lett.*, vol. 31, no. 23, pp. 3462–3464, Dec. 2006, doi: 10.1364/OL.31.003462.

[87] A. Liero, A. Klehr, S. Schwertfeger, T. Hoffmann, and W. Heinrich, "Laser driver switching 20 A with 2 ns pulse width using GaN," in *IEEE MTT-S Int. Microw. Symp. Dig.*, May 2010, pp. 1110–1113.

[88] T. Hoffmann, A. Klehr, A. Liero, G. Erbert, and W. Heinrich, "Compact high-current diode laser nanosecond-pulse source with high efficiency and 13 μJ output energy," *Electron. Lett.*, vol. 51, no. 1, pp. 83–85, Jan. 2015, doi: 10.1049/el.2014.3204.

[89] M. Žbik and P. Wieczorek, "Charge-line dual-FET high-repetition-rate pulsed laser driver," *Appl. Sci.*, vol. 9, no. 7, p. 1289, Mar. 2019, doi: 10.3390/app9071289.

[90] E. Abramov, M. Evzelman, O. Kirshenboim, T. Urkin, and M. M. Peretz, "Low voltage sub-nanosecond pulsed current driver IC for high-resolution LIDAR applications," in *Proc. IEEE APEC*, Jun. 2018, pp. 708–715.

[91] S. Vainshtein, V. Zemlyakov, V. Egorkin, A. Maslevtsov, and A. Filimonov, "Miniature high-power nanosecond laser diode transmitters using the simplest possible avalanche drivers," *IEEE Trans. Power Electron.*, vol. 34, no. 4, pp. 3689–3699, Apr. 2019, doi: 10.1109/TPEL.2018.2853563.

[92] S. Arslan, S. A. A. Shah, and H. Kim, "Power efficient current driver based on negative boosting for high-speed lasers," *Electronics*, vol. 8, no. 11, p. 1309, Nov. 2019, doi: 10.3390/electronics8111309.

[93] S. Rigault, N. Moeneclaey, L. Labrak, and I. O'Connor, "CMOS VCSEL driver dedicated for sub-nanosecond laser pulses generation in SPAD-based time-of-flight rangefinder," in *Proc. DCIS*, 2018, pp. 1–6.

[94] A. Tajfar, M. Zamprogno, F. Villa, and F. Zappa, "A 20 a sub-nanosecond integrated CMOS laser diode driver for high repetition rate SPAD-based direct Time-of-Flight measurements," in *Proc. ICCECE*, 2018, pp. 272–276.

[95] J. S. Glaser, "High power nanosecond pulse laser driver using a GaN FET," in *Proc. PCIM*, 2018, pp. 662–669.

[96] C. Wang, S. Zhuo, and C. Liu, "A CMOS laser driver with configurable optical power for time-of-flight 3D-sensing," in *Proc. IEEE 3rd Int. Conf. Integr. Circuits Microsyst. (ICICM)*, Nov. 2018, pp. 25–28, doi: 10.1109/ICAM.2018.8596490.

[97] J. S. Glaser, "Kilowatt laser driver with 120 a, sub-10 nanosecond pulses in <3 cm using an GaN FET," in *Proc. PCIM*, Jun. 2018, pp. 39–44.

[98] G. Blasco, D. Dorich, E. Isern, R. Burkard, and E. Martin, "An 80 a, 2 to 25 ns configurable pulse-width integrated CMOS pulsed laser driver with on-chip mounted laser diode," in *Proc. IEEE Int. Symp. Circuits Syst. (ISCAS)*, Oct. 2020, pp. 1–5.

[99] M. Wens, J. M. Redoute, T. Blanchaert, N. Bleyaert, and M. Steyaert, "An integrated 10 A, 2.2 ns rise-time laser-diode driver for LIDAR applications," in *Proc. ESSCIRC*, Nov. 2009, pp. 144–147, doi: 10.1109/ESSCIRC.2009.5326005.

[100] *Design and Test of Fast Laser Driver Circuits*, iC-Haus GmbH, Bodenheim, Germany, 2012.

[101] G. Barrere, "Measuring transformer coupling factor K," Exality Corp., Tech. Rep., 2010.

[102] M. B. Del Alamo, C. Soncco, R. Helaconde, J. L. B. Alba, and A. M. Gago, "Laser spot measurement using simple devices," *AIP Adv.*, vol. 11, no. 7, Jul. 2021, Art. no. 075016, doi: 10.1063/5.0046287.

[103] L. Svilainis and V. Dumbrava, "Numerical comparison of LED directivity approximation functions for video displays," *Displays*, vol. 31, nos. 4–5, pp. 196–204, Dec. 2010, doi: 10.1016/j.displa.2010.08.001.

[104] D. A. Hutchins, R. J. Dewhurst, and S. B. Palmer, "Directivity patterns of laser-generated ultrasound in aluminum," *J. Acoust. Soc. Amer.*, vol. 70, no. 5, pp. 1362–1369, 1981, doi: 10.1121/1.387126.

[105] I. Arias and J. D. Achenbach, "Thermoelastic generation of ultrasound by line-focused laser irradiation," *Int. J. Solids Struct.*, vol. 40, no. 25, pp. 6917–6935, Dec. 2003.

[106] I. A. Veres, T. Berer, and P. Burgholzer, "Numerical modeling of thermoelastic generation of ultrasound by laser irradiation in the coupled thermoelasticity," *Ultrasonics*, vol. 53, no. 1, pp. 141–149, Jan. 2013, doi: 10.1016/j.ultras.2012.05.001.

[107] L. Svilainis, V. Dumbrava, S. Kitov, A. Aleksandrovas, P. Tervydis, and D. Liaukonis, "Electronics for ultrasonic imaging system," *Elektron. Elektrotech.*, vol. 20, no. 7, pp. 51–56, 2014, doi: 10.5755/j01.eee.20.7.8024.

[108] M. Pollakowski, H. Ermert, L. von Bernus, and T. Schmeidl, "The optimum bandwidth of chirp signals in ultrasonic applications," *Ultrasonic*, vol. 31, no. 6, pp. 417–420, Nov. 1993.

[109] F. Honarvar, H. Sheikhzadeh, M. Moles, and A. N. Sinclair, "Improving the time-resolution and signal-to-noise ratio of ultrasonic NDE signals," *Ultrasonics*, vol. 41, no. 9, pp. 755–763, 2004.